

Ultralow-field nuclear magnetic resonance for direct nondestructive observation of electrolyte composition in batteries

Anne M. Fabricant^{a,b,c,1}, Román Picazo-Frutos^{a,b,c,2}, Florin Teleanu^{d,e,f}, Gregory J. Rees^{g,h}, Robert A. House^{g,h}, Peter G. Bruce^{g,h,i}, John Blanchard^j, James Eills^k, Kirill Sheberstov^l, Dmitry Budker^{a,b,c,m}, Danila A. Barskiy^{a,b,c}, and Alexej Jerschow^{f,3}

This manuscript was compiled on August 12, 2024

Rechargeable batteries represent a key transformative technology for electric vehicles, portable electronics, and renewable energy. Despite enormous developments in battery research, there are few nondestructive diagnostic techniques compatible with realistic commercial cell enclosures. Many battery failures result from the loss or chemical degradation of electrolyte. Here we show measurements through battery enclosures that allow quantification of electrolyte amount, composition, and potentially degradation. This study employs instrumentation and techniques developed in the context of zero-to-ultralow-field nuclear magnetic resonance (ZULF NMR), with optical atomic magnetometers as the detection elements. In contrast to conventional NMR methodology, the reduced background magnetic fields employed here make even potentially thick stacks of battery housing and electrodes transparent to the lower-frequency electromagnetic fields involved. Both the solvent and lithium-salt components of the electrolyte signature can be quantified, as the results described herein demonstrate.

rechargeable battery | NMR | electrolyte | nondestructive testing | atomic magnetometry

Rechargeable batteries, especially lithium-ion batteries, are already enabling great leaps in the electrification of transportation and in the use of alternative energy sources. High-field NMR of battery materials is a rich area of research, and many relevant electrochemical processes have been studied with this technique (1–4). One pain point of current technology, however, is the limited ability of analytical or diagnostic techniques to detect changes or defects within realistic battery cells (as opposed to purely research cells) in a nondestructive fashion. Recently, magnetic resonance imaging (MRI) was adapted to sense changes in the structure or magnetic susceptibility of battery materials, and thereby to provide a link between external measurements and internal processes in batteries (5–8). This type of indirect approach was further demonstrated with magnetometry, where atomic magnetometers were used to detect changes in the induced field as a function of applied background magnetic field (9)—specifically showing, for example, nonuniform lithium incorporation into the cathode. Further extensions of MRI- and magnetometry-based approaches to battery diagnostics include the detection of small (μA) currents either during charging/discharging or during resting periods (9), as well as the use of alternative detection media (10). Other types of sensors/modalities, such as magnetically induced tomography detected by nitrogen-vacancy (NV) centers in diamond (11) allowed access to further observables for battery assessment. All these techniques provided the ability to probe either changes in solid components as a function of Li incorporation, or changes in electrical current distributions through the measurement of magnetic fields around the batteries.

The electrolyte itself has so far not received much attention in the aforementioned approaches to nondestructive testing, nor was it generally possible to detect changes in electrolyte composition directly. The nature, distribution, and composition of the electrolyte are, however, critically important to the proper functioning of a cell. Changes such as leakage or electrolyte degradation due to aging processes are frequently the reason for battery failures (12–14).

Typical battery electrolytes are composed of a solvent—often a mixture of ethylene carbonate (EC) with dimethyl carbonate (DMC)—and the solute, a Li salt such as LiPF_6 . In this work, we aimed to study common battery-cell enclosures containing these chemicals, in order to access the characteristic spectroscopic signatures that would allow quantification of electrolyte amount and composition, including LiPF_6 content. The measurement of electrolytes through aluminum

Significance Statement

Many technological advances, such as the electrification of transportation or the use of alternative energy sources, require the availability of reliable rechargeable batteries. How can we tell a good battery from a bad one? How can we determine the reason for battery failure? Answers to these questions are surprisingly difficult to obtain, largely due to a lack of proper battery-diagnostic techniques. In this work, we demonstrate an ultralow-field spectroscopic method for nondestructive sensing of the state of a battery electrolyte. Because the electrolyte forms a critical component of a rechargeable battery cell, and electrolyte loss or degradation is a common battery failure mode, the presented techniques provide critical device data.

Author affiliations: ^aInstitute of Physics, Johannes Gutenberg University of Mainz, 55099 Mainz, Germany; ^bHelmholtz Institute Mainz, 55099 Mainz, Germany; ^cGSI Helmholtzzentrum für Schwerionenforschung, 64291 Darmstadt, Germany; ^dExtreme Light Infrastructure - Nuclear Physics, “Horia Hulubei” National Institute for Physics and Nuclear Engineering, 077125 Bucharest, Romania; ^eInterdisciplinary School of Doctoral Studies (ISDS), University of Bucharest, 050663 Bucharest, Romania; ^fDepartment of Chemistry, New York University, New York, NY 10003, USA; ^gDepartment of Materials, University of Oxford, Oxford OX1 6NN, UK; ^hThe Faraday Institution, Didcot, OX11 0RA, UK; ⁱDepartment of Chemistry, University of Oxford, Oxford OX1 3TA, UK; ^jQuantum Technology Center and Institute for Research in Electronics & Applied Physics, University of Maryland, College Park, Maryland 20742, USA; ^kIBEC - Institute for Bioengineering of Catalonia, Barcelona Institute of Science and Technology, 08028 Barcelona, Spain; ^lLaboratoire des Biomolécules, LBM, Département de Chimie, École Normale Supérieure, PSL University, Sorbonne Université, CNRS, 75005 Paris, France; ^mDepartment of Physics, University of California, Berkeley, CA 94720, USA

A.M.F., R.P.F., G.J.R., J.B., J.E., K.S., D.A.B., and A.J. designed research; A.M.F., R.P.F., F.T., and G.J.R. performed research; G.J.R., R.A.H., and P.G.B. contributed samples; A.M.F., R.P.F., F.T., and D.A.B. analyzed data; D.A.B., D.B., and A.J. supervised the project; A.M.F., R.P.F., F.T., G.J.R., and A.J. wrote the paper; all authors edited the paper.

Competing interest statement: Authors have filed the provisional U.S./E.U. patent, application number 63649837, “Battery electrolyte characterization using low-field nuclear magnetic resonance”.

¹A.M.F. and ²R.P.F. contributed equally to this work.

³To whom correspondence should be addressed. E-mail: alexej.jerschow@nyu.edu

enclosures is of particular interest, as Al is the typical housing for the commercial flat Li-ion pouch and prismatic cells widely used in electric vehicles, portable electronics, and renewable-energy storage (15).

One option for obtaining spectroscopic electrolyte signatures from the inside of a cell is to examine it with nuclear magnetic resonance (NMR). At the frequencies commonly employed in NMR spectroscopy (hundreds of MHz), however, the skin depth of electromagnetic radiation in metal is only on the order 10 μm , which prevents fields from penetrating the cell during nuclear-spin excitation and detection. Although demonstrations at such high frequencies exist, quantification and reproducibility are challenging due to field-shaping effects and tuning variabilities (16, 17). Because skin depth scales inversely with the square root of frequency (Fig. S1), even low-field benchtop instruments (based on permanent magnets, with proton precession frequencies on the order 10 MHz) still only enable penetration of tens of μm of metal at best. For this reason, and due to sample-size limitations, battery testing with benchtop NMR is typically limited to studies of research pouch cells which fit into an NMR tube, or to inline studies of redox flow cells (18). By contrast, in zero-to-ultralow-field (ZULF) NMR experiments (Fig. 1), the resonance frequencies of nuclear-spin samples can span the range from Hz to kHz and are tunable through the application of a background field. Spin excitation is typically performed using pulses of static magnetic fields, and metals are therefore essentially transparent to the applied and measured electromagnetic waves.

In traditional NMR spectroscopy, internal couplings and especially J -couplings—indirect spin-spin couplings mediated by the electrons shared in chemical bonds—are much smaller than the Zeeman interaction. In the ZULF-NMR regime, the situation is opposite: the Zeeman interaction is much weaker than the J -coupling interaction, such that Zeeman coupling represents a small perturbation to the J -coupling Hamiltonian. Thus, rather than molecular information being encoded in chemical-shift values, the angular-momentum selection rules give rise to so-called J -spectra (19, 20). These spectra can be used to obtain molecular fingerprints of studied samples. ZULF-NMR spectra are also practically unaffected by field drifts and inhomogeneities, and consequently display narrower spectral lines compared to higher-field measurements (21, 22). Furthermore, they do not suffer from susceptibility-induced line broadening even in materials with complex internal structure (23).

At the relatively low frequencies of signals in ZULF-NMR spectroscopy, inductive detection is largely ineffective due to decreased sensitivity, so detection is typically performed with either superconducting quantum-interference devices (SQUIDs) (24) or (noncryogenic) atomic magnetometers, also called optically pumped magnetometers (OPMs) (25). Both SQUIDs and the most sensitive atomic magnetometers require operation in a near-zero-field environment, where Earth's magnetic field is screened by means of magnetic shielding. Furthermore, to boost signals, nonequilibrium spin polarization of samples is created either by prepolarizing them in a stronger magnetic field (using a permanent magnet or electromagnet) or by employing hyperpolarization techniques (26). With these implementations, ZULF NMR has been successfully applied to studies of fundamental

physics (27, 28), chemical fingerprinting of biological samples and metabolism using J -spectroscopy (21, 22, 29), as well as relaxometry at hypogeomagnetic fields (30, 31). Battery diagnostics represent a new direction using ZULF-NMR instrumentation.

To demonstrate the sensitivity of our method to the smallest possible realistic volume of battery electrolyte, experiments were performed on Al battery enclosures containing tens of μL of electrolyte. As shown in the following, we found that examination of the measured spectra allowed the detection and assignment of electrolyte signals such that concentrations, as well as changes in composition and potentially degradation, could be quantified.

Results and Discussion. In this work, we employ a ZULF-NMR setup based on thermal prepolarization, mechanical shuttling between the prepolarization and measurement regions, and room-temperature, quadrature detection using commercially available atomic magnetometers (32). The general experimental apparatus and measurement scheme are described in (31). Figure 1 shows the apparatus as used in the experiments presented here; further details are provided in the Materials and Methods as well as Supporting Information (SI). Photos of the measured sample cells, along with the cell holder, are shown in Fig. S2.

The electrolytes selected for this study were composed of different amounts of LiPF_6 dissolved in a 50:50vol% mixture of EC/DMC (Fig. 1B). In ZULF-NMR spectra, one therefore expects to observe a lower-frequency family of signals—depending on the background field and associated Larmor precession frequencies—which arise from Li^+ , PF_6^- , and the EC/DMC solvent protons (henceforth referred to as the near-zero-frequency peaks, “nZF-peaks”). In addition, the PF_6^- unit gives rise to transitions at higher frequencies of $\frac{3}{2}J_{\text{PF}}$, $\frac{5}{2}J_{\text{PF}}$, and $\frac{7}{2}J_{\text{PF}}$, where $J_{\text{PF}} \approx 710$ Hz is the J -coupling constant between ^{31}P and ^{19}F nuclei (20) (signals referred to as the “ J -peaks” in the following). See Fig. 2A and Fig. S3 for energy-level diagrams.

For the implementation of our method, we chose to focus on the nZF-manifold for two reasons: (1) the J -peaks are approximately 200 times weaker than the nZF-peaks for PF_6^- , which would complicate the measurement of smaller sample volumes within a reasonable amount of time; (2) the higher frequencies of the J -peaks fall outside the sensitive bandwidth of the magnetometers used in this study (signals are detectable up to 500 Hz, with flat sensor response in a 100 Hz band (32)).

Figure 2 shows a characteristic electrolyte spectrum measured from a sample cell at a background field of 2.7 μT . Although nZF-peaks could in principle be measured at arbitrarily low background fields, practical considerations motivated a choice of field in the microtesla range, corresponding to a ^1H Larmor frequency of approximately 115 Hz; all PF_6^- and EC/DMC signals appear within the spectral range 86–130 Hz. This approach allowed us to move the signals of interest out of a lower-frequency region where significant noise was observed due to shuttling of the conductive aluminum housing (Fig. S4). The complexity of the PF_6^- nZF-manifold is readily reproduced by simulations using the Spinach package in Matlab (33) (Fig. 2) and stems from lifting the degeneracy inside spin manifolds due to the Zeeman perturbation of ZULF eigenstates (34, 35)—as

249
250
251
252
253
254
255
256
257
258
259
260
261
262
263
264
265
266
267
268
269
270
271
272
273
274
275
276
277
278
279
280
281
282
283
284
285
286
287
288
289
290
291
292
293
294
295
296
297
298
299
300
301
302
303
304
305
306
307
308
309
310

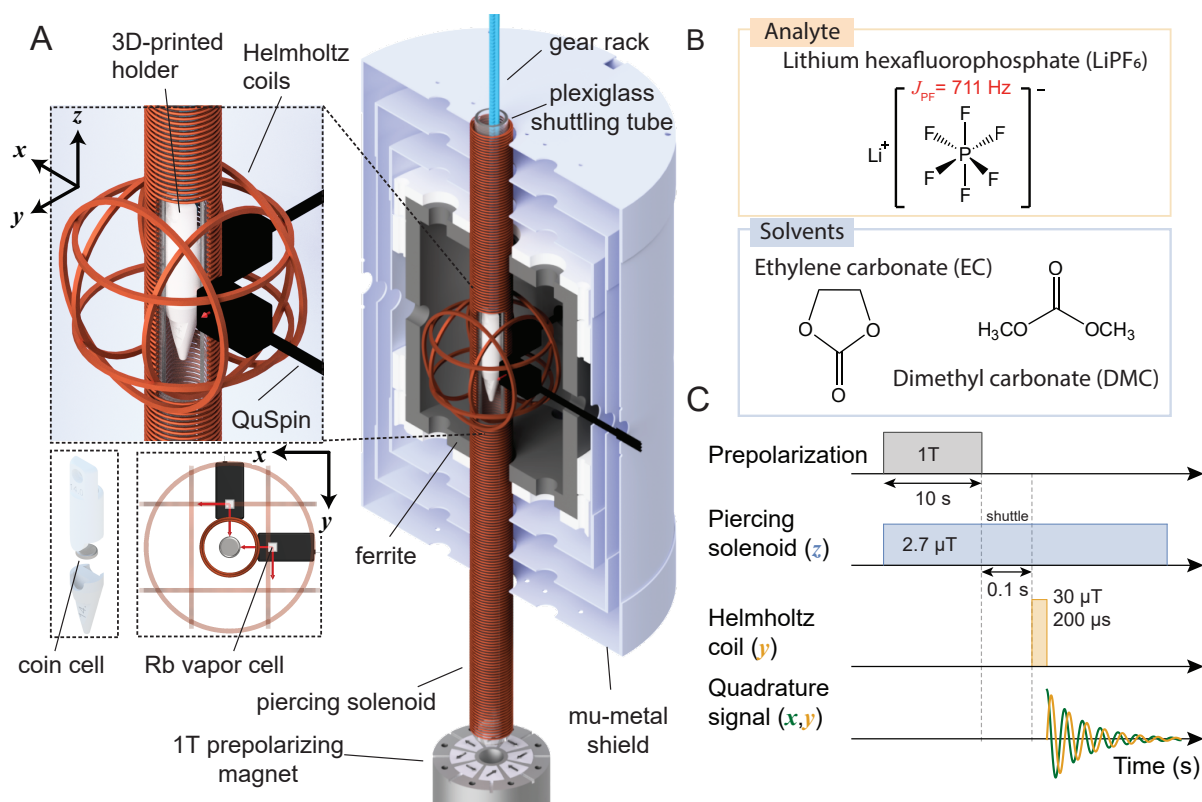


Fig. 1. (A) Experimental ultralow-field NMR apparatus for mechanically shuttling thermally nuclear-spin-polarized samples to a hypogeomagnetic measurement region, where spin manipulation and subsequent measurement take place. Cut-out shows the plastic holder containing a sample cell inside the piercing solenoid, where a tunable measurement field is used to produce magnetic resonances detected by atomic magnetometers (sensitive axes indicated by the four red arrows). The general shuttling setup was described in (31), and further details of the specific operation of this apparatus are provided in Materials and Methods. (B) Electrolyte (solvent and solute/analyte) chemical compositions studied in this work. (C) Measurement sequence for a single signal readout (or “scan”) including prepolarization, shuttling, application of a 90° magnetic-field pulse to rotate magnetization into the detection plane, and detection of a decaying magnetic-dipole signal as the magnetization precesses freely in the applied solenoid field. Finally, the sample is shuttled back to the prepolarizing magnet for the next scan. Experiments typically consisted of many scans which were averaged to improve the measured signal-to-noise ratio (SNR) of electrolyte signals from sample cells containing less than 100 μL of electrolyte.

illustrated in Fig. 2. A simulation of the EC/DMC proton signal is also included, as well the measured water-proton signal from a calibration cell filled with deionized water. Finally, the background signal from an empty cell is displayed to identify artifacts not arising from the spin sample, such as the noise peak at 84 Hz. The sample volume was only about 80 μL , and it is thus quite promising that electrolyte NMR signals can be obtained from such a small volume using atomic magnetometers. For completeness, we note that we were also able to identify the Li^+ signal at lower frequency, here around 45 Hz (Fig. S5C). For subsequent analysis, however, the signals of PF_6^- and EC/DMC were used, since they had larger SNR and were farther away from spectral noise features.

In order to consistently extract electrolyte concentrations from all recorded experimental spectra, solute and solvent signals were integrated over the shaded regions indicated in Fig. 2—including the two largest PF_6^- peaks in an 8 Hz spectral window centered around 93.38 Hz, and the solvent proton peak in an 8 Hz spectral window centered around 101.32 Hz. Although the latter integration region also contains a smaller PF_6^- signal at 116 Hz, this contribution is negligible compared to the much larger (by two orders of magnitude) proton signal.

Figure 3A presents the spectra for a series of samples prepared with different electrolyte concentrations and approximately the same total liquid content. The bottom trace in Fig. 3A was acquired using a reference vial of known electrolyte concentration. In Fig. 3B, the solute and solvent signals are compared for each sample based on the integrals extracted from the indicated shaded spectral regions. The ratio of integrated solute and solvent signals was compared to the signals from the calibration-vial data (Fig. 3A and SI Fig. S5A) in order to obtain normalized concentration values. Figure 3C shows the calculated PF_6^- concentration for all cells, normalized to the 2 M calibration sample, following the relation

$$C_{\text{PF}_6^-} = \left(\frac{S[\text{PF}_6^-]}{S[\text{solvent}]}\right) \times \left(\frac{S^{\text{vial}}[\text{PF}_6^-]}{S^{\text{vial}}[\text{solvent}]}\right)^{-1} \times (2 \text{ M}) . [1]$$

Here, S is the measured signal (integrated area of the peak, Fig. 3B). We chose this calibration approach in part because the total liquid amount in each cell varied due to the production method (in the process of sealing the cells, some spillage was inevitable). Therefore, comparing signal ratios between the samples and reference vial data allowed us to remove uncertainty arising from different liquid amounts or potential leakage. The signal from the vial is much larger than

311
312
313
314
315
316
317
318
319
320
321
322
323
324
325
326
327
328
329
330
331
332
333
334
335
336
337
338
339
340
341
342
343
344
345
346
347
348
349
350
351
352
353
354
355
356
357
358
359
360
361
362
363
364
365
366
367
368
369
370
371
372

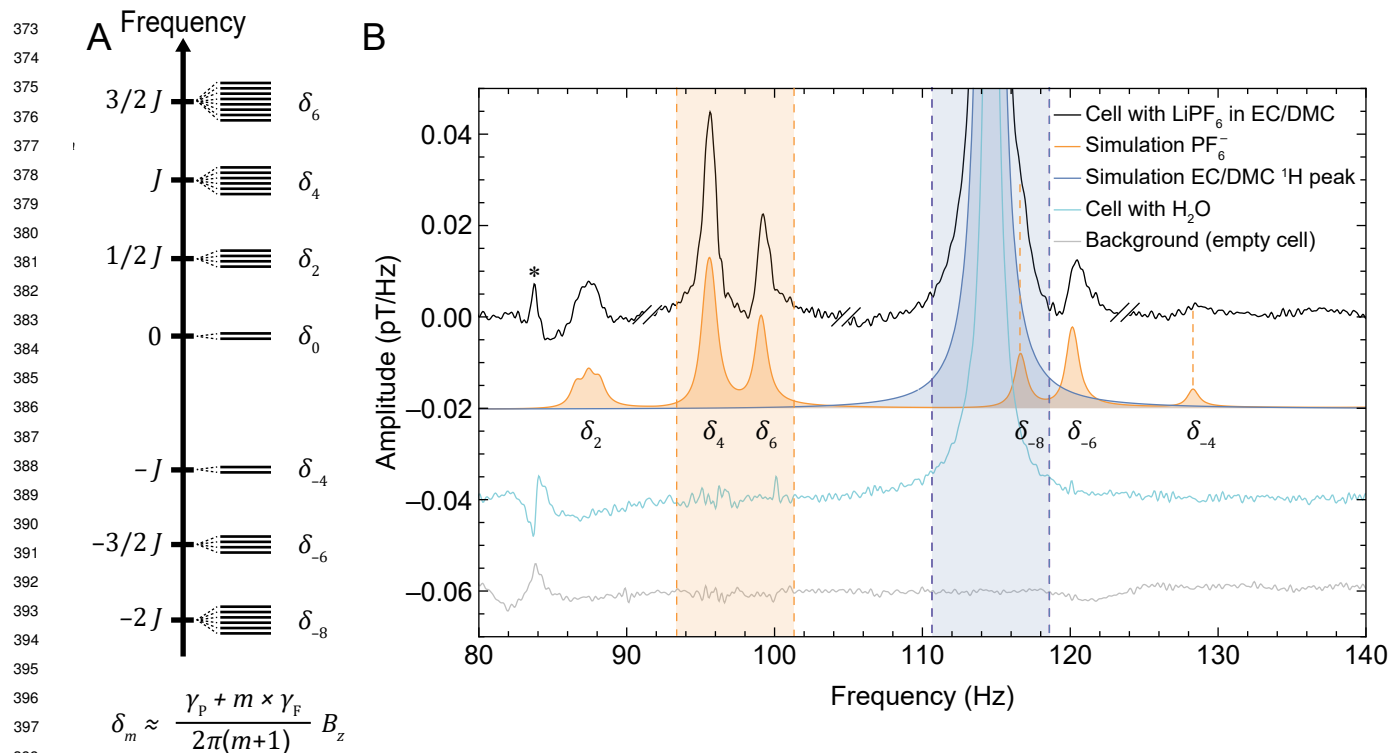


Fig. 2. (A) Energy-level diagram showing manifolds containing eigenstates of the J -coupling Hamiltonian for the PF_6^- spin system (see SI for further details). Application of a background magnetic field B_z in the solenoid (Fig. 1) lifts the degeneracy of the eigenstates within each manifold, splitting the energy levels as indicated schematically. Each δ_m , where m is an integer, refers to the transition frequency between energy levels of the same manifold. Here, $J = 711$ Hz and the Zeeman splitting is approximately linear in the ultralow field regime; γ_P and γ_F are the gyromagnetic ratios of phosphorus and fluorine, respectively. (B) Characteristic measured and simulated NMR signals at a $2.7 \mu\text{T}$ background magnetic field. The graph displays the recorded electrolyte signature from a sample cell (black), a background noise measurement of an empty cell (gray), simulation of the PF_6^- spin system (orange), simulation of the solvent proton signal (blue), and a recorded spectrum from an identical cell containing deionized water for calibration (cyan). The near-zero-frequency (nZF) peaks corresponding to the δ_m transitions are labeled beneath the simulated spectrum. Experimental spectra are obtained from averages of 10 000 scans. The shaded areas indicate the frequency ranges used for calculation of concentrations, as described in the main text. Electrolyte experimental data (black) was phased using the relative zero-order phases -30° , 150° , 0° , and -90° in four different spectral regions, respectively (see Materials and Methods and SI); double dashes delimitate these phased regions. The spectra are offset for visual clarity, and vertical orange dashed lines provide an aid to the eye for the measured PF_6^- peaks with lower SNR. The SNR of the PF_6^- peaks are 13, 74, 37, 20, and 5 for the peaks at approximately 87, 96, 99, 115, 120, and 128 Hz, respectively—calculated as the maximum signal amplitude divided by the standard deviation of a neighboring noise region from 132 to 140 Hz. The linewidths (full width at half maximum, FWHM) of these peaks range from 1 to 1.5 Hz.

that from the sample cells (Fig. 3A), due to both an increased sample volume (the vial contained 1.5 mL of electrolyte while the cells typically contained $\sim 80 \mu\text{L}$) and a more efficient geometry (the sensor arrangement depicted in Fig. 1 is more suitable for the approximately cylindrical geometry of the vial, rather than the disc-like coin cells). These factors, as well as possible demagnetization effects due to fields induced by shuttling conductive material (see SI), do not affect the relative quantification method of Eq. (1). For samples 3 and 4, the SNR of electrolyte signals, barely visible in Fig. 3A, are relatively low, and hence the calculated concentrations have larger error bars in Fig. 3C.

To demonstrate the robustness of our setup and the reproducibility of measurements, we analyzed partitions of data from the same (largest-SNR) sample at different time intervals under identical experimental conditions, as displayed in Fig. 4. The standard errors of solute and solvent signals extracted from this data set were used to calculate the error bars displayed in Fig. 3. In this analysis, uncertainty on measured signals (peak integrals) is assumed to scale inversely with SNR, such that higher SNR corresponds to a smaller error bar (see SI for further details). These error bars account

for both statistical uncertainty as well as possible systematic uncertainty over the course of the measurement cycle.

As is evident from Fig. 3C comparing the measured LiPF_6 concentrations to the nominal (prepared) concentrations, for the majority of samples, the measured concentrations agree with the nominal values to within 10%. Furthermore, the relative stability or loss/leakage of electrolyte signals could be tracked through time-separated measurement of the same cells (Figs. S6 and S7.) Only samples 6 and 7 display larger deviations between nominal and measured concentrations—this could be attributable to production systematics or the fact that signal size and linewidth may affect the percentage of peak area contained within the integration bounds.

Finally, to test compatibility of the experimental setup and protocol not only with Al housing but also with all other components of a realistic working battery, additional custom sample cells were tested—without electrolyte but containing a copper current collector, a lithium anode, a glass-fiber separator, and a lithium-nickel-manganese-cobalt-oxide (NMC811) cathode. Although the inclusion of copper material may increase the amount of background noise attributed to shuttling-induced eddy currents (Fig. S8), this is not expected

497
498
499
500
501
502
503
504
505
506
507
508
509
510
511
512
513
514
515
516
517
518
519
520
521
522
523
524
525
526
527
528
529
530
531
532
533
534
535
536
537
538
539
540
541
542
543
544
545
546
547
548
549
550
551
552
553
554
555
556
557
558

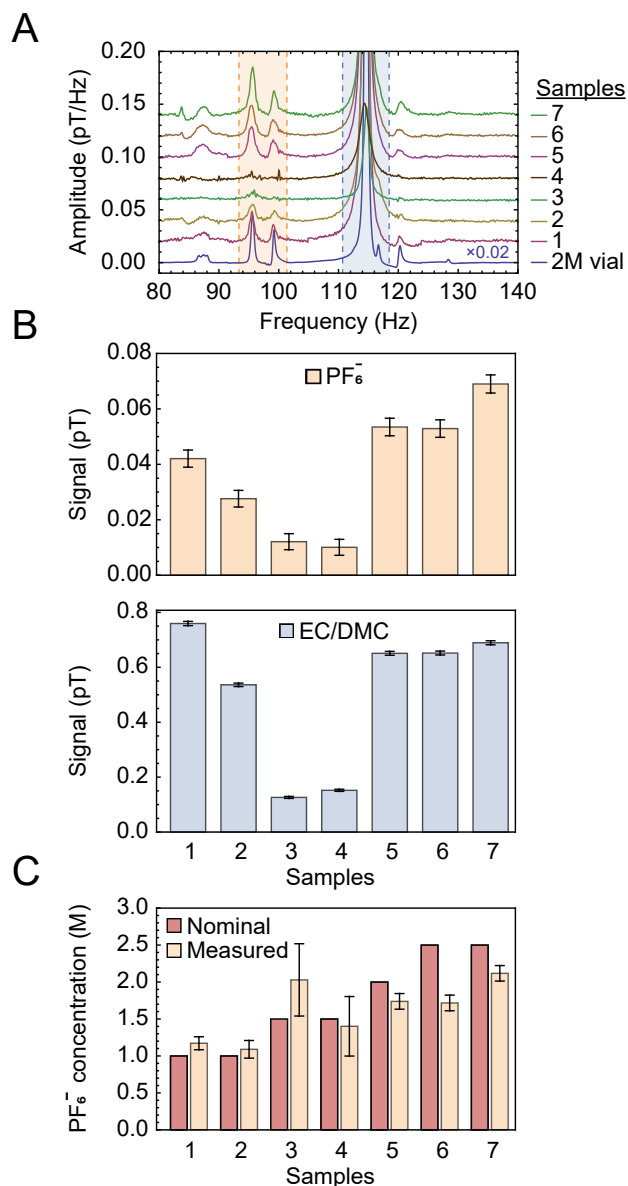


Fig. 3. (A) Stacked plots showing the measured electrolyte signals at a 2.7 μ T background field from a series of sample cells filled with electrolyte of different nominal (prepared) LiPF₆ concentrations. All spectra were obtained from averages of 10 000 scans, apart from sample 1 and the calibration vial for which 8913 and 256 scans were collected, respectively; the large number of scans was selected to improve SNR of measured signals from the cells, as well as to suppress the power-line harmonic at 100 Hz. (B) Quantification of signals obtained from integration of the shaded areas indicated in A for the solute and solvent peaks (top and bottom panels, respectively). Error bars correspond to the standard errors obtained in Fig. 4 and their values as a fraction of the signal scale inversely with SNR, as explained in the main text. (C) LiPF₆ concentrations obtained from the measurements in (B) and propagation of errors, according to the procedure outlined in the main text.

559
560
561
562
563
564
565
566
567
568
569
570
571
572
573
574
575
576
577
578
579
580
581
582
583
584
585
586
587
588
589
590
591
592
593
594
595
596
597
598
599
600
601
602
603
604
605
606
607
608
609
610
611
612
613
614
615
616
617
618
619
620

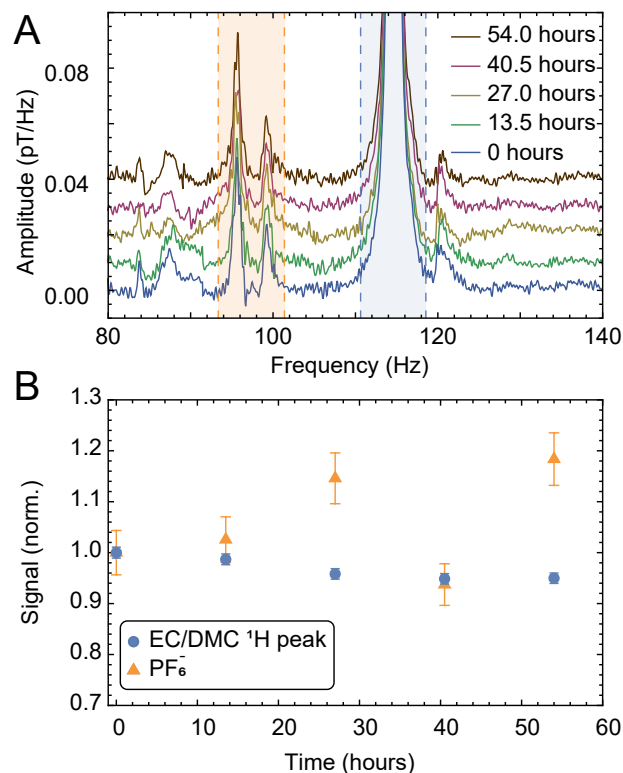


Fig. 4. Monitoring of the electrolyte peaks as a function of time, using five partitions or batches of 2000 scans (13.5 h each) from the cell with a nominal 2.5 M LiPF₆ concentration (sample 7). (A) Measured spectra, and (B) solute and solvent integrals normalized to the first data point. Error bars are calculated as standard error of the partitioned integrated signals (shaded regions). The error on the proton signal is smaller than that on the PF₆⁻ signal (relative errors of 4.4% and 1.1% for solute and solvent signals, respectively), as expected due to the smaller SNR of the latter. The electrolyte signals from this sample cell were found to be relatively stable not only over the course of the three-day measurement cycle (with minor fluctuations), but also in a second measurement taken two months later (Fig. S6).

to prevent measurement or characterization of electrolyte content, since the noise occurs at lower frequencies. Thus, we believe that our work paves the way to measurements of commercial pouch or prismatic cells via adaptation of the polarizing magnet and experimental geometry.

Envisioned experimental enhancements for battery-diagnostic applications include optimization of the measurement duty cycle for faster sensitive detection of electrolyte (Fig. S8), reduction of the sensor offset distance using customized atomic magnetometers, and optimization of the shuttling field profile to maximize SNR. One may also use a superconducting magnet (~ 20 T) for prepolarization to immediately achieve a 20-fold boost in signal (see SI) and a speed-up in data collection by a factor of 400.

In future studies, J -peaks may also be detected directly or indirectly. Indirect detection could be enabled via prior population transfer, whereby one resonantly irradiates J -transitions and subsequently detects a signal enhancement of the n ZF-peaks. Such an approach may further enable the identification of chemical species and degradation products in the electrolyte (Fig. S12). Further diagnostic potential is attainable from measurement of spectral linewidths. Cathode degradation may occur due to transition metal dissolution, and the presence of paramagnetic Ni^{2+} and Mn^{2+} ions in solution could be identified via their effect on lineshape broadening (36). Finally, cycling of battery cells is expected to be associated with additional degradation and consumption of the electrolyte during cycling. For example, cracking of the cathode material can expose fresh surface area with which the electrolyte reacts, thereby consuming the electrolyte (14) and affecting the spectral signature.

Conclusion. We have demonstrated the ability of ultralow-field NMR spectroscopy to directly characterize battery electrolyte composition through battery housing, in a manner compatible with nondestructive operando measurements. NMR signals were recorded using atomic magnetometers. The quantification and characterization of electrolytes is crucial for the diagnosis of battery defects and aging processes. The work is easily extendable to a large class of electrolytes and battery geometries beyond those examined here. Nondestructive battery diagnostics remain extremely limited, and the addition of this method provides critical characterization capability for battery development and testing.

Materials and Methods

The sample cells forming the primary data set of this article were manufactured in February 2024 and measured March–April 2024. Additional experimental results, calibration data, simulations, and photographs are available in SI.

Instrumentation and data collection. The experimental setup (Fig. 1A) and SNR-enhancing “gradiometric quadrature” detection method are described in detail in (31), where device calibration and applications of proton relaxometry were discussed. In this work, the apparatus was operated at a constant background field of $2.7 \mu\text{T}$ along $-\hat{z}$ inside the double-layer piercing solenoid, corresponding to an applied current of $600 \mu\text{A}$ and a proton precession frequency of 114.6 Hz (Fig. 2). Prior to measurement, each sample cell was enclosed in a 3D-printed PLA holder affixed to the plastic gear rack and positioned inside the 1 T permanent magnet (Halbach array). A single measurement cycle (Fig. 1C) consisted of: (1) 10 s nuclear-spin polarization in the magnet, (2) 100 ms shuttling 36 cm into the detection region at the center of the magnetic shield (Twinleaf MS1-LF), (3) application of a $30 \mu\text{T}$ $\pi/2$ magnetic-field pulse along

$-\hat{y}$ to rotate magnetization into the x - y detection plane (Fig. S11), (4) at least 5 s four-channel acquisition of the free-induction-decay (FID) signal by two dual-axis QuSpin Zero-Field Magnetometers (QZFM Gen-2) during magnetization precession in the background field, and (5) return of the sample to the starting position inside the magnet. One sensor was pointing along the x -direction and the other along the y -direction, to enable quadrature detection (31). The cylindrical cell holder (Fig. S2) has outer diameter 14 mm and inner diameter 10 mm. In a typical experiment, 10 000 scans were averaged, a $200 \mu\text{s}$ pulse was applied to both proton and PF_6^- spin systems (Fig. S11), and the duty cycle was ~ 20 s with several seconds of rest between scans. Calibration data was collected using 1.5 mL cylindrical glass calibration vials with interior dimensions approximately 10 mm (diameter) by 20 mm (height).

Battery samples. The AG7 coin-cell cases were constructed from ultra-pure aluminium metal (99.9%). Lithium hexafluorophosphate (LiPF_6 (s)) salt was dissolved into a 50v:50v mixture of ethylene carbonate (EC: $(\text{CH}_2\text{O})_2\text{CO}$ (s)) and dimethyl carbonate (DMC: $\text{OC}(\text{OCH}_3)_2$ (l)), to form 0.5, 1 (LP30), 1.5, 2, and 2.5 M salt concentration electrolytes. A total of $\sim 80 \mu\text{L}$ of the various-concentration electrolytes was then pipetted into each of the coin-cell cases. The coin cells were sealed using a homemade plastic insert, to prevent magnetic impurities from the coin-cell crimper. All samples were stored, handled, and processed in an argon atmosphere (<1 ppm O_2 and H_2O). Each sealed cell had an outer diameter of 9.4 mm and height 2.6 mm (Fig. S2); the average thickness of the side wall through which electrolyte signals were measured was around 1 mm. The interior dimensions of the cells were approximately 7.3 mm (diameter) by 2 mm (height).

Data processing. The production of gradiometric quadrature frequency spectra from the raw magnetometer time traces was carried out using Matlab according to the procedure described in (31), and further postprocessing for lineshape correction, peak phasing, and integration/quantification was implemented in Mathematica (see SI for further details). All spectra were phased by joining sections with different first-order phases as described in the caption of Fig. 3.

ACKNOWLEDGMENTS. We thank Dr. Piotr Put for assistance in development of the experimental apparatus and software, Dr. Peter Blümler for providing the polarizing magnet, and Chengtong Zhang for helping with sample preparation. This research was supported in part by DFG grant BU 3035/15-1. A.J. acknowledges funding from the Carl-Zeiss-Humboldt Research Award and a grant from the US National Science Foundation, number CHE 2108205. F.T. acknowledges funding through a Fulbright Fellowship from the Romanian-U.S. Fulbright Commission. G.J.R. is grateful to the Royal Society for the Royal Society Short Industry Fellowship. P.G.B. is indebted to the EPSRC, the Henry Royce Institute for Advanced Materials (EP/R00661X/1, EP/S019367/1, EP/R010145/1, and EP/L019469/1), and the Faraday Institution (FIRG016) for financial support. R.A.H. acknowledges funding from the Royal Academy of Engineering under the Research Fellowship scheme. D.A.B. acknowledges support from the Alexander von Humboldt Foundation in the framework of the Sofja Kovalevskaja Award.

745		807
746		808
747		809
748	1. CP Grey, N Dupré, NMR studies of cathode materials for lithium-ion rechargeable batteries. <i>Chem. Rev.</i> 104 , 4493–4512 (2004).	810
749	2. NM Trease, L Zhou, HJ Chang, BY Zhu, CP Grey, In situ NMR of lithium ion batteries: Bulk susceptibility effects and practical considerations. <i>Solid State Nucl. Magn. Reson.</i> 42 , 62–70 (2012).	811
750		812
751	3. O Pecher, J Carretero-González, KJ Griffith, CP Grey, Materials' methods: NMR in battery research. <i>Chem. Mater.</i> 29 , 213–242 (2017).	813
752		814
753	4. X Liu, et al., Solid-state NMR and MRI spectroscopy for Li/Na batteries: Materials, interface, and in situ characterization. <i>Adv. Mater.</i> 33 , 2005878 (2021).	815
754	5. S Chandrashekar, et al., 7Li MRI of Li batteries reveals location of microstructural lithium. <i>Nat. Mater.</i> 11 , 311–315 (2012).	816
755		817
756	6. AJ Ilott, NM Trease, CP Grey, A Jerschow, Multinuclear in situ magnetic resonance imaging of electrochemical double-layer capacitors. <i>Nat. Commun.</i> 5 , 4536 (2014).	818
757	7. AJ Ilott, M Mohammadi, HJ Chang, CP Grey, A Jerschow, Real-time 3D imaging of microstructure growth in battery cells using indirect MRI. <i>Proc. Natl. Acad. Sci.</i> 113 , 10779–10784 (2016).	819
758		820
759	8. AJ Ilott, M Mohammadi, CM Schauerman, MJ Ganter, A Jerschow, Rechargeable lithium-ion cell state of charge and defect detection by in-situ inside-out magnetic resonance imaging. <i>Nat. Commun.</i> 9 , 1776 (2018).	821
760		822
761	9. Y Hu, et al., Sensitive magnetometry reveals inhomogeneities in charge storage and weak transient internal currents in Li-ion cells. <i>Proc. Natl. Acad. Sci.</i> 117 , 10667–10672 (2020).	823
762		824
763	10. K Romanenko, PW Kuchel, A Jerschow, Accurate visualization of operating commercial batteries using specialized magnetic resonance imaging with magnetic field sensing. <i>Chem. Mater.</i> 32 , 2107–2113 (2020).	825
764		826
765	11. X Zhang, et al., Battery characterization via eddy-current imaging with nitrogen-vacancy centers in diamond. <i>Appl. Sci.</i> 11 , 3069 (2021).	827
766		828
767	12. T Taskovic, et al., Alkyl dicarbonates, common electrolyte degradation products, can enable long-lived Li-ion cells at high temperatures. <i>J. The Electrochem. Soc.</i> 170 , 090527 (2023).	829
768	13. Z Ye, et al., Impact of salts and linear carbonates on the performance of layered oxide/hard carbon sodium-ion pouch cells with alkyl carbonate electrolytes. <i>J. The Electrochem. Soc.</i> (2024).	830
769		831
770	14. CR Birkel, MR Roberts, E McTurk, PG Bruce, DA Howey, Degradation diagnostics for lithium ion cells. <i>J. Power Sources</i> 341 , 373–386 (2017).	832
771		833
772	15. A Kwade, et al., Current status and challenges for automotive battery production technologies. <i>Nat. Energy</i> 3 , 290–300 (2018).	834
773	16. BJ Walder, et al., NMR spectroscopy of coin cell batteries with metal casings. <i>Sci. Adv.</i> 7 (2021).	835
774		836
775	17. S Benders, M Mohammadi, CA Klug, A Jerschow, Nuclear magnetic resonance spectroscopy of rechargeable pouch cell batteries: Beating the skin depth by excitation and detection via the casing. <i>Sci. Reports</i> 10 , 13781 (2020).	837
776		838
777		839
778		840
779		841
780		842
781		843
782		844
783		845
784		846
785		847
786		848
787		849
788		850
789		851
790		852
791		853
792		854
793		855
794		856
795		857
796		858
797		859
798		860
799		861
800		862
801		863
802		864
803		865
804		866
805		867
806		868